Design of GaSb-based monolithic passive photonic devices at wavelengths above 2 μm

Journal of Physics: Photonics

OPEN ACCESS

RECEIVED
16 March 2023

REVISED
21 June 2023

ACCEPTED FOR PUBLICATION
6 July 2023

PUBLISHED
18 July 2023

PAPER

Design of GaSb-based monolithic passive photonic devices at wavelengths above 2 μm

Md Saiful Islam Sumon[1], Shrivatch Sankar[1], Weicheng You[1], Imad I Faruque[2], Sarvagya Dwivedi[3] and Shamsul Arafin[1,*]

[1] Department of Electrical and Computer Engineering, The Ohio State University, Columbus, OH, United States of America
[2] Quantum Engineering Technology Laboratories (QET Labs), University of Bristol, Bristol, United Kingdom
[3] Rockley Photonics, Pasadena, CA, United States of America
[*] Author to whom any correspondence should be addressed.

E-mail: arafin.1@osu.edu

Keywords: directional coupler, multimode interferometer, Y-branch, power splitters, grating coupler, photonic integrated circuit, mid-wave infrared (MWIR)

Supplementary material for this article is available online

Abstract

In this paper, we report, for the first time, a theoretical study on passive photonic devices including optical power splitters/combiners and grating couplers (GCs) operating at non-telecom wavelengths above 2 μm in a monolithic GaSb platform. Passive components were designed to operate, in particular, at around 2.6 μm for monolithic integration with active photonic devices on the III–V gallium antimonide material platform. The three popular types of splitters/combiners such as directional couplers, multimode interferometer-, and Y-branch-couplers were theoretically investigated. Based on our optimized design and rigorous analysis, fabrication-compatible 1 $\times$ 2 optical power splitters with less than 0.12 dB excess losses, large spectral bandwidth, and a 50:50 splitting ratio are achieved. For fiber-to-chip coupling, we also report the design of GCs with an outcoupling efficiency of $\sim$29% at 2.56 μm and a 3 dB bandwidth of 80 nm. The results represent a significant step towards developing a complete functional photonic integrated circuits at mid-wave infrared wavelengths.

1. Introduction

The mid-wave infrared (MWIR) wavelength regime of the electromagnetic spectrum is of significant interest because it contains a number of spectral features such as strong overtones and combination molecular absorption bands in gas- and liquid-phase molecules. This is beneficial for a wide range of emerging applications including chemical and biological sensing [1, 2], and non-invasive medical diagnosis [3]. Especially, the 2.5 μm to 2.63 μm wavelength range of the MWIR regime is important due to the presence of strong water vapor (H_2O), hydrogen-sulfide (H_2S), hydrogen cyanide (HCN) and nitrous oxide (N_2O) absorption lines, enabling photonic sensors to detect these gases at a much higher selectivity and sensitivity [4]. By taking advantage of this inherent molecular selectivity and considering the huge application opportunities, establishing MWIR photonic sensor technologies at the chip scale as integrated low-cost solutions is immediately evident.

Photonic integrated circuits (PICs), containing active and passive photonic components connected with low-loss passive waveguides, are of utmost importance for implementing such on-chip photonic sensors. As far as material platforms for monolithic integrated PICs are considered, InP and its alloys are less attractive due to material limitations for making photonic devices at the intended extended short (S)-MWIR wavelength regime [5]. The recent success of silicon photonics at telecom wavelengths and silicon-on-insulator's (SOI's) transparency up to 3.5 μm could pave the way for a passive SOI waveguiding platform [6]. But the challenges of achieving high-performance semiconductor lasers and complicated laser-Si waveguide integration processes at S-MWIR wavelengths make the SOI platform less reliable. Although GaSb-based materials are relatively less mature, they comprise the optimal material system for realizing long-wavelength

active devices such as lasers and photodetectors. When it comes to waveguides, the GaSb material system is fully transparent at $\lambda > 2$ μm, confirming low material absorption [5]. The latter requires a vertical-etch profile and smooth sidewall which could be achieved by the recent advancement of dry- and wet-etch processes in this material system [7].

Various optical passive components at S-MWIR [8, 9] wavelengths were demonstrated using SOI up to 3.5 μm [10] and in Ge-on-Si up to 8.5 μm [11]. There are also few demonstrations of heterogeneously integrated InP gain materials on silicon PICs reported around 2.3 μm [12]. MWIR PICs have recently been demonstrated using heterogeneous integration of GaSb-based interband cascade lasers (ICLs) with SOI passive components [13, 14]. However, the preliminary integrated device performance was limited in part by the greater technological challenge of bonding GaSb to silicon, followed by processing the laser ridges from the back, and by the inefficient transfer of laser power from the 'hybrid' GaSb/silicon waveguide of the gain region to a passive silicon waveguide. Tapers employed in the integrated ICLs to date have induced much more reflection (in addition to scattering and absorption losses) than the transmission of the laser beam propagating in the hybrid waveguide. This is probably due to the requirement for an abrupt evolution of the mode and mismatch of modes in the hybrid and silicon waveguides.

A monolithic GaSb platform alleviates these problems through the tight integration of both passive and active components on GaSb as a host substrate material. This will also provide an optimal path toward strongly suppressing laser instabilities associated with unintended external feedback. In this work, we present the designs of various passive components including power splitters/combiners and grating couplers (GCs) on GaSb substrates. As a center operating wavelength, ~2.56 μm was chosen to develop this new integrated circuit technology. Some of the key factors behind this wavelength selection include knowledge availability of good type-I gain medium with no miscibility gap and the resulting high-performance active devices including lasers and photodetectors at this specific wavelength [12, 15]. All these can be ensured by the well-studied InGaAsSb/GaSb active region-based lasers emitting around 2.56 μm with a record-low threshold current density at infinite lengths [12, 15, 16]. This will eventually help achieve complete functional PICs with a tight integration of active and passive devices in the future. In this study, directional coupler (DC)-, multimode interferometer (MMI)-, and Y-branch-based splitters were designed and analyzed for this wavelength. GCs at the same wavelength were also investigated for in- and outcoupling light from waveguides. The development of missing but fundamentally realistic passive devices on GaSb by monolithically integrating active components is expected to have a great impact on the way toward implementing complete functional long-wavelength PICs.

2. Design and waveguide details

In this work, single-mode waveguides and power splitters at 2.56 μm were designed and their performance was evaluated using finite difference eigenmode (FDE) and eigenmode expansion (EME) solvers, respectively, whereas GCs were optimized using the 3D finite-difference time-domain (FDTD) solver by employing commercial software Ansys Lumerical [17].

We considered surface ridge waveguides (except GCs) as they are ideally suited for active devices because of high current confinement, moderate optical confinement, and lower loss in single-mode waveguides [18]. The surface ridge waveguide based on GaSb-based epitaxial layers is schematically shown in figure 1(a). The thickness of the both bottom n- and top p-doped AlGaAsSb cladding layers is 2 μm, while the core GaSb material is 450 nm. Figure 1(b) shows the intensity profile of fundamental TE mode (TE_0) of the 4 μm ridge with $n_{eff} = 3.62$. The spatial refractive index profile of the waveguide materials is shown in figure 1(c). Details of the waveguide design could also be found elsewhere [5].

Figure 1(d) shows the effective refractive indices n_{eff} of the few lowest order guided TE and TM modes as a function of the ridge width W. Up to a width of 2.4 μm, the waveguide supports only single TE modes. However, in experiments, devices with wider widths are found to emit a single fundamental mode. The first higher-order odd mode TE_1 in a laser cavity receives very little gain due to a null at the waveguide center and is not usually considered while defining the single-mode waveguide cut-off condition [19]. TM modes were also not considered since the III–V laser structure employs compressively-strained quantum wells which favor only TE-polarized light. Thus the calculated ridge width supporting single mode is 4.4 μm, as represented by the vertical dashed line.

3. Results and discussion

With the goal of demonstrating high-performance GaSb-based passive PICs at MWIR wavelengths, we consider three popular types of power splitters/combiners. While choosing one of the types, one considers several key performance metrics that include form factor, insertion loss, variable splitting ratio, fabrication

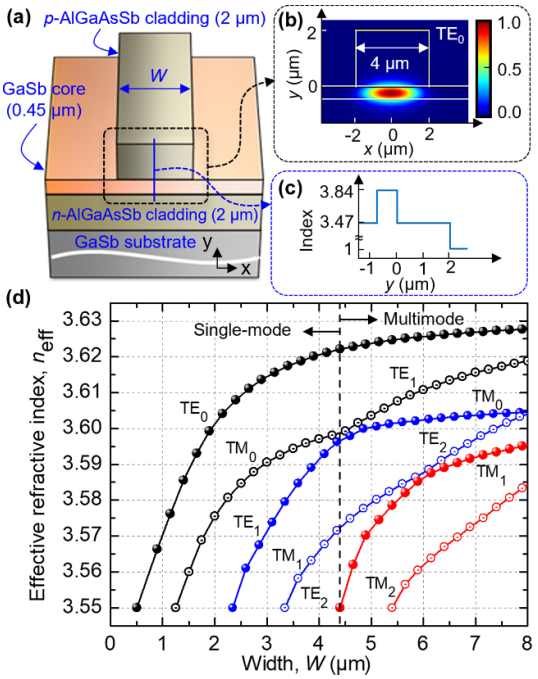

Figure 1. (a) Schematic cross-section of the GaSb-based single-mode surface ridge waveguide, (b) fundamental TE_0 mode at 2.56 μm, (c) material refractive index vs position along the transverse direction, and (d) mode effective index as a function of waveguide width, *W*.

tolerance, phase difference between the power at output arms, and wide bandwidth operation. Since each type cannot provide all these advantageous features at the same time, performance parameters are prioritized based on the targeted applications where PICs will be used for.

3.1. Directional coupler (DC)

DCs are formed by placing two waveguides in parallel where the coupling coefficient is determined not only by the coupler's length but also by the distance between the waveguides. A 3D schematic of GaSb-based DC is shown in figure 2(a). The simplified cross-over length $L'_{50\%}$ for coupling half of the light to the second waveguide from the input waveguide can be obtained from equation (1),

$$L'_{50\%} = \frac{\lambda}{4\Delta n} \tag{1}$$

where Δn is the difference between the effective indices of the first two eigenmodes of coupled waveguides commonly termed as symmetric and antisymmetric supermodes [20]. By numerical calculation of supermodes, Δn is obtained as 0.0033 considering that the waveguides are placed 0.2 μm apart as shown in figure 2(a). Thus, $L'_{50\%}$ becomes 196 μm for the abruptly placed parallel waveguides that were corrected to $L_{50\%} = L'_{50\%} + L_{\text{bend}}$, where, L_{bend} represents the effective additional coupler length required for collecting light at the bar and cross ports. L_{bend} is calculated to be 76 μm, yielding $L_{50\%} = 272$ μm. The calculated coupling gaps between the waveguides before and after the cubic Beizer curve representing the S-bend are 0.2 μm and 8 μm, respectively. Further design details and physical analysis of the DCs can be found in the supplementary document. Note that the waveguide width of the DCs is 4 μm which can easily be resolved by standard optical lithography. However, a coupling gap of 0.2 μm which may require electron beam lithography (EBL). By reducing the waveguide width at the coupling section, it is possible to increase the coupling gap while maintaining a fixed coupling length. This design opens the possibility of utilizing standard optical photolithography [21] to effectively fabricate the desired DC structures.

Figure 2(b) presents the electric field intensity profile of our designed DCs at 2.56 μm, which shows 50% splitting of the input power. The transmission, excess loss, and splitting ratio of the bar port of the proposed DCs are shown in figure 2(c). At 2.56 μm, we achieve 50:50 transmission to the output ports along with an excess loss of 0.05 dB mainly due to waveguide and bending losses. Figure 2(c) also illustrates that achieving a 50:50 splitting ratio is only feasible if operated at 2.56 μm for the designed dimension. Consequently, it is evident that utilizing a DC coupler for light splitting is impractical when a broadband operation is essential. Figure 2(c) shows the trends of the bar and cross port transmission as well as the excess loss for the designed

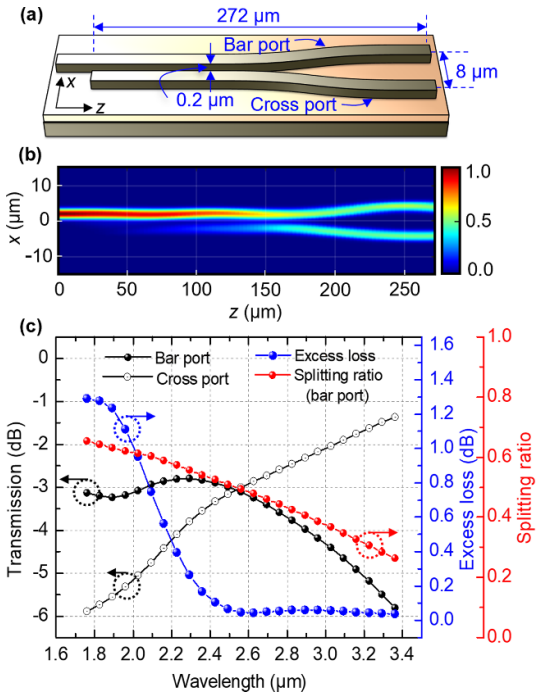

Figure 2. (a) 3D schematic of the designed directional coupler, (b) electric field intensity at 2.56 μm wavelength, and (c) transmission, excess loss, and splitting ratio of the bar port for 1.6 μm wide wavelength range centering 2.56 μm of the proposed DC.

DC. As the operating wavelength decreases from 2.56 μm, the transmission for the bar port does not increase as expected, while the excess loss increases. This behavior is due to the increased effective index of the fundamental mode at lower wavelengths, leading to higher mode confinement within the waveguide and reduced optical energy transfer from the bar port to the cross port. Lower wavelengths also result in more excess loss due to a large number of higher-order modes for a fixed waveguide width of 4 μm. Conversely, for higher wavelengths, the excess loss remains low due to the 4 μm waveguide (higher than the fundamental limit) width which allows good performance up to 3.36 μm. However, at higher wavelengths, the bar port transmission decreases since the coupling length is fixed for 50:50 coupling at 2.56 μm. Although the 50:50 splitting is obtained only at 2.56 μm as anticipated, the DCs show a 1 dB bandwidth of >1 μm for different splitting ratios. Our design also confirms an inherent 90° phase shift due to 50% coupling at the cross port relative to the input port.

To achieve operation over a wide range of wavelengths with a fixed splitting ratio, we designed the other two types of power splitters.

3.2. Multimode interferometer (MMI)

MMI couplers based on the self-imaging effect [22], are crucial in PICs as they provide a wide range of possible input and output ports that control the splitting/combining capabilities. MMI couplers are preferred when fabrication constraints are considered compared to other types of splitters [23]. Our GaSb-based MMI power splitter has a multimode region whose width, $W_{\mathrm{MMI}} = 15$ μm as shown in figure 3(a). The core width of the MMI region supports the first three even TE modes. Analytical self-imaging length, L_{MMI} and the length at which N number of images are formed, $L_{1\times N}$ can be obtained from equations (2) and (3), respectively,

$$L_{\mathrm{MMI}} = \frac{n_{\mathrm{eff},y} \times W_{\mathrm{MMI}}^2}{\lambda} \tag{2}$$

$$L_{1\times N} = \frac{L_{\mathrm{MMI}}}{N} + \Delta L \tag{3}$$

where, $n_{\mathrm{eff},y}$ is the effective index of the slab waveguide formed in the transverse direction at the core, λ is the wavelength, N is an integer, and ΔL is the excess length considered to compensate for Goos–Hänchen effect that causes little penetration of light into the cladding region [24]. Using the effective index method, $n_{\mathrm{eff},y}$ is found to be 3.62 for the GaSb-based MMI splitter at $\lambda = 2.56$ μm. Thus equation (2) gives $L_{\mathrm{MMI}} = 318.5$ μm

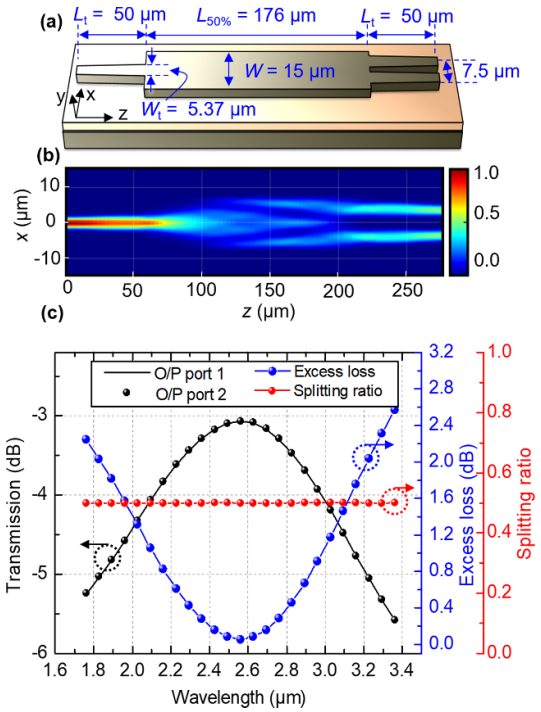

Figure 3. (a) 3D schematic of the designed MMI, (b) electric field intensity at 2.56 μm wavelength, and (c) transmission, excess loss, and splitting ratio for 1.6 μm wide wavelength range centering 2.56 μm of the optimized MMI.

and a distance of $L_{MMI}/2$ gives two images. By the EME method, $L_{1\times2}$ is obtained as 176 μm thus a correction of $\Delta L = 16.7$ μm is required to compensate for the Goos–Hänchen effect [24]. A linear taper at the input and output waveguides helps reduce the excess loss by decreasing the waveguide and multimode region mode mismatch [23]. A taper at the input and output sections of the MMI with length L_t and width, W_t are optimized, which are 50 μm and 5.37 μm, respectively. The optimal in-plane dimension corresponds to a tapering angle of 0.79°, resulting in the lowest excess loss. Two output ports of the MMI coupler are separated by $W_{MMI}/2$, i.e. 7.5 μm. Further design details and physical analysis of the MMIs can be found in the supplementary document. Note that the minimum feature size in the MMIs is 4 μm waveguide at the input and output arms and a minimum required gap is more than 2 μm between the output arms which can be written in an optical photolithography tool [21].

Figure 3(a) shows the 3D schematic of the proposed optimized MMI-based power splitter with all the dimensions labeled. The electric field intensity profile at 2.56 μm wavelength of the proposed GaSb-based 1 × 2 MMI coupler is shown in figure 3(b). The transmission, excess loss, and splitting ratio of the proposed MMI coupler are shown in figure 3(c). At 2.56 μm, we achieve 50:50 transmission to the output ports along with an excess loss of 0.055 dB mostly contributed by the waveguide loss at the single and multimode sections. Figure 3(c) also shows that for different wavelengths other than 2.56 μm, 50% splitting is also possible but the excess loss will be higher as suggested by the blue dotted curve. Besides, figure 3(c) demonstrates that our proposed MMI coupler can achieve a 1 dB bandwidth of greater than 0.9 μm with no change in the splitting ratio.

3.3. Y-branch

The 1 × 2 Y-branch splitters consist of one input waveguide with a power splitting junction in the middle connected to two output waveguides. The output waveguides consist of S-bends to carry the mode without creating any back reflection within the waveguide. The single mode of input ports transitions to a symmetric mode of the double waveguide system with a dip in the center, and this then transitions to two separate modes in each waveguide. For combining, the situation is reversed if the energy from the two waveguides is in-phase, as in a Mach–Zehnder during on-state. The power combining can also be low-loss, although still with some finite loss (due to the required radiation loss). As the modes from the two waveguides begin to overlap, one gets a 'supermode' for the two waveguides, which is the symmetric mode of the two-channel waveguide.

Figure 1(a) presents the basic schematic of the tapered branch Y junction beam splitter. To achieve equal outputs at the Y-branch, a linear and slow taper of from 4 μm to 8.2 μm was considered followed by two

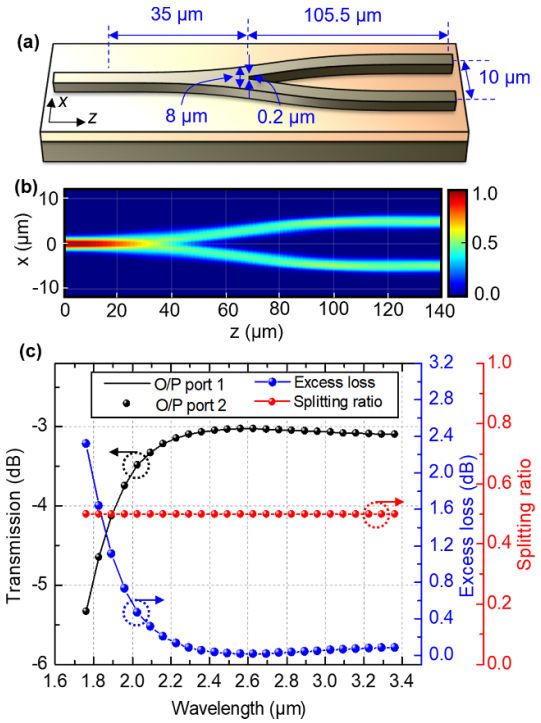

Figure 4. (a) 3D schematic of the designed Y-branch, (b) electric field intensity at 2.56 μm wavelength, and (c) transmission, excess loss, and splitting ratio for 1.6 μm wavelength range centering 2.56 μm of the optimized Y-branch.

optimized S-bends separated by 10 μm at the output ends. The taper broadens the mode causing less back-reflection from the junction and the S-bend reduces the insertion loss by compensating the mode bending caused by the Y-junction. The optimized taper and S-bend lengths are obtained as 35 μm and 105.5 μm, respectively. The tip near the Y-junction is 0.2 μm wide, requiring EBL to resolve. By increasing the tip width to 0.6 μm at the junction, it becomes feasible to fabricate the structures using standard optical photolithography [21], albeit with a slight sacrifice in terms of loss.

Since the SOI platform has a core-cladding index contrast of more than five times compared to our structure, the low-loss splitter at 1.55 μm was achieved with a compact Y-junction [25] which is seven times smaller in geometric dimensions than our designed couplers at 2.56 μm. To achieve low insertion loss in the SOI platform, a genetic algorithm was employed to optimize the widths of the Y-branch at different positions of the junction [20, 26]. However, in our specific case, employing this approach leads to a considerable increase in device length due to width variations caused by a lower refractive index contrast in a vertical direction. The electric field intensity profile of the proposed GaSb-based 1 $\times$ 2 Y-branch is shown in figure 4(b). The transmission, excess loss, and splitting ratio as a function of the wavelength of the designed Y-branch are superposed in figure 4(c). We obtain 50:50 transmission to the output ports along with an excess loss of 0.12 dB for an output arm separation of 0.2 μm for the wavelength of 2.56 μm. However, the loss increases to 0.66 dB if the separation is 0.6 μm due to the increased radiation loss at the junction. Figure 4(c) also illustrates that the desired 50:50 splitting is achieved at 2.56 μm wavelength with minimal excess loss. Importantly, this splitting characteristic is maintained at other wavelengths, confirming its broadband operation. Its 1 dB bandwidth is calculated to be $\geqslant$1 μm as the waveguide also works considerably well for longer wavelengths due to its large ridge width. Unlike DCs, it maintains a fixed splitting ratio even though the loss is more than MMI and DC. Further design details and physical analysis of the Y-branch splitters can be found in the supplementary materials.

3.4. Vertical grating coupler (VGC)

Due to the significant modal size mismatch, efficient coupling between a single-mode fiber and waveguide is difficult. Two commonly used approaches to overcome this issue are VGC (off-plane) and edge coupler (in-plane). Although the coupling efficiency (CE) and bandwidth of GCs are usually less compared to edge couplers, they are more attractive due to their measurement and alignment flexibilities, wafer-level testing conveniences, and comparatively compact size [27]. In a GC, a propagating mode usually encounters four principal loss mechanisms including diffracted light towards top cladding, substrate leakage, back reflection, and the power transmitted through the grating for an outcoupling to fiber case. Only a part of the first of

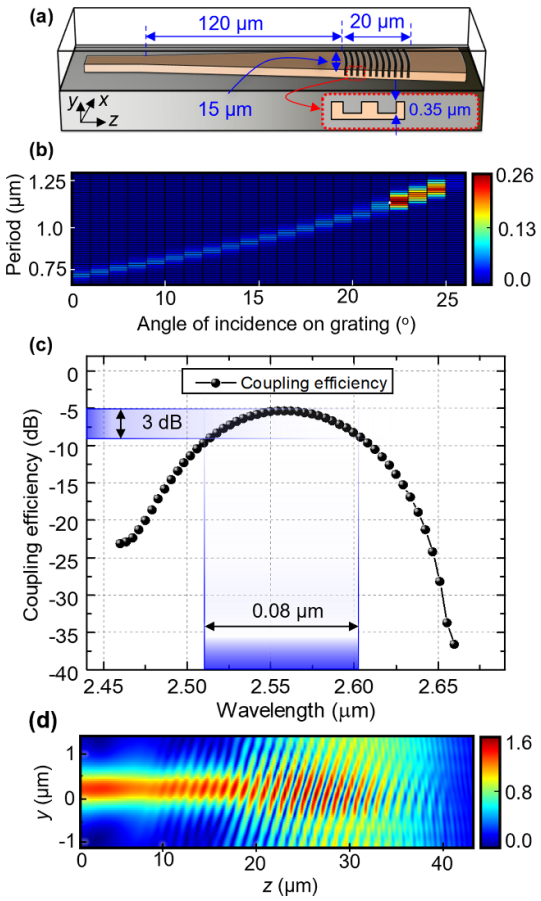

Figure 5. (a) 3D schematic of the designed vertical grating coupler, (b) normalized power transmission as a function of grating period and angle of incidence on the grating, (c) electric field intensity at 2.56 μm wavelength, and (d) normalized transmission for 0.2 μm wavelength range centering 2.56 μm.

these four contributes to the coupling and others act as loss which can be minimized but not eliminated [28]. These loss factors become more prominent in the III–V platform due to low vertical index contrast compared to the SOI platform.

We designed uniform GCs with a linear taper using buried channel waveguides where core is fully-etched and the top 2 μm thick cladding encapsulates patterned core structures. A focusing design was adopted to reduce the footprint of our GCs. Considering the mode field diameter of the commercially-available ZrF_4 fiber [29], we designed a grating region with 15 μm × 20 μm as shown in figure 5(a) for the wavelength of 2.56 μm. An optimized taper length of 120 μm is required, yielding 0.11 dB loss due to a slight mode mismatch at the taper output side, which also determines the focusing radius of the gratings to be 120 μm. Considering an etch depth of 0.35 μm and fixed fiber position, the CE for different combinations of the angle of incidence on the grating (5°–25°) and grating period are obtained. The CE contour in figure 5(b) shows that the maximum CE is obtained when light is incident at 22° on the grating, which necessitates a 60° angle of incidence on the top cladding. A grating period of ∼1.13 μm provides the maximum CE. For a fill factor of 0.5, both the minimum feature size (ungrated region) and gap (grated region) are 0.565 μm, compatible with a low-cost optical lithography process [21]. The simplified analytical grating formula (equation (4)) provides the grating period p, when the wavelength λ, diffraction mode number m, the average effective refractive index of the grated and ungrated regions n_{eff}, index of cladding n_{clad}, and the fiber angle θ are known [20],

$$p = \frac{m\lambda}{n_{\text{eff}} - n_{\text{clad}} \times \sin\theta} \tag{4}$$

$$n_{\text{eff}} = \text{ff} \times n_{\text{eff},1} + (1 - \text{ff}) \times n_{\text{eff},2} \tag{5}$$

where $n_{\text{eff},1} = 3.62$, $n_{\text{eff},2} = 3.5$ are the effective refractive indices of the grated and ungrated regions, respectively for the present design using the designed etch depth and fill factor, ff of 0.5. For the 1st-order diffraction mode at 22° in the cladding, equations (4) and (5) yield $p = 1.13$ μm. Thus, the grating equation

supports our FDTD design of the GC. Further design details and physical analysis of the GCs can be found in the supplementary document.

Figure 5(c) shows the CE of the GC as a function of wavelengths for a 0.2 μm range centering 2.56 μm. The CE vs wavelength curve also shows that a maximum CE of −5.4 dB or 28.7% is achieved at the target wavelength of 2.56 μm. Figure 5(c) also shows that a simulated 3 dB bandwidth of 80 nm is achievable in our designed GC. Figure 5(d) shows the mode profile across the grating region, confirming light coupling from the fiber to the waveguide through the grating. This cross-sectional side view of the electric field intensity profiles at 2.56 nm confirms the GC principle that relies on the constructive and destructive interference resulting from the wavefronts generated through the diffraction of light by grating teeth.

4. Conclusion

In this article, we proposed 1 × 2 optical power splitters based on DC, MMI, and Y-branch along with a VGC on the GaSb platform. The power splitters are of low excess loss ($\leqslant$0.12 dB) and operate for a wide range of wavelengths with an excellent power uniformity of two output ports at wavelengths above 2 μm. The proposed GC has a CE of ∼29% at 2.56 μm. Our design study is expected to contribute significantly to monolithic PICs at other extended S-MWIR wavelengths as well.

Data availability statement

The data cannot be made publicly available upon publication because no suitable repository exists for hosting data in this field of study. The data that support the findings of this study are available upon reasonable request from the authors.

Acknowledgment

This work was supported by the National Science Foundation (NSF) under Grant 2144375.

Conflict of interest

The authors have no conflicts to disclose.

ORCID iD

Shamsul Arafin https://orcid.org/0000-0003-4689-2625

References

[1] Peng C, Yang C, Zhao H, Liang L, Zheng C, Chen C, Qin L and Tang H 2023 Optical waveguide refractive index sensor for biochemical sensing *Appl. Sci.* **13** 3829
[2] Elkhazraji A, Shakfa M K, Abualsaud N, Mhanna M, Sy M, Marangoni M and Farooq A 2023 Laser-based sensing in the long-wavelength mid-infrared: chemical kinetics and environmental monitoring applications *Appl. Opt.* **62** A46
[3] Darwich M A, Shahen A, Daoud A, Lahia A, Diab J and Ismaiel E 2023 Non-invasive IR-based measurement of human blood glucose *Eng. Proc.* **35** 27
[4] Gordon I E *et al* 2017 The HITRAN 2016 molecular spectroscopic database *J. Quant. Spectrosc. Radiat. Transfer* **203** 3–69
[5] You W, Dwivedi S, Faruque I I, John D D, McFadden A P, Palmstrøm C J, Coldren L A and Arafin S 2023 Towards GaSb-based monolithically integrated widely-tunable lasers for extended short-and mid-wave infrared wavelengths *IEEE J. Quantum Electron.* **59** 1–9
[6] Zou Y, Chakravarty S, Chung C-J, Xu X and Chen R T 2018 Mid-infrared silicon photonic waveguides and devices *Photon. Res.* **6** 254–76
[7] Arafin S, McFadden A P, Paul B, Hasan S M, Gupta J A, Palmstrøm C J and Coldren L A 2019 Study of wet and dry etching processes for antimonide-based photonic ICs *Opt. Mater. Express* **9** 1786–94
[8] Roelkens G, Dave U D, Gassenq A, Hattasan N, Hu C, Kuyken B, Leo F, Malik A, Muneeb M and Ryckeboer E 2014 Silicon-based photonic integration beyond the telecommunication wavelength range *EEE J. Sel. Top. Quantum Electron.* **20** 394–404
[9] Rouifed M-S, Littlejohns C G, Tina G X, Haodong Q, Hu T, Zhang Z, Liu C, Reed G T and Wang H 2016 Low loss SOI waveguides and MMIs at the MIR wavelength of 2 μm *IEEE Photonics Technol. Lett.* **28** 2827–9
[10] Stirling C J, Cao W, Reynolds J D, Qu Z, Bradley T D, Mastronardi L, Gardes F Y and Nedeljkovic M 2022 Mid-infrared silicon-on-insulator waveguides with single-mode propagation over an octave of frequency *Opt. Express* **30** 8560–70
[11] Lim J, Shim J, Kim I, Kim S K, Lim H, Ahn S-Y, Park J, Geum D-M and Kim S 2023 Low-loss and high-confinement photonic platform based on germanium-on-insulator at mid-infrared range for optical sensing *J. Lightwave Technol.* **41** 1–11
[12] Wang R, Vasiliev A, Muneeb M, Malik A, Sprengel S, Boehm G, Amann M-C, Šimonytė I, Vizbaras A and Vizbaras K 2017 III–V-on-silicon photonic integrated circuits for spectroscopic sensing in the 2–4 μm wavelength range *Sensors* **17** 1788
[13] Spott A, Stanton E J, Torres A, Davenport M L, Canedy C L, Vurgaftman I, Kim M, Kim C S, Merritt C D and Bewley W W 2018 *Heterogeneously Integrated Interband Cascade Lasers On* (IEEE) pp 1–2

[14] Spott A, Stanton E J, Torres A, Davenport M L, Canedy C L, Vurgaftman I, Kim M, Kim C S, Merritt C D and Bewley W W 2018 Interband cascade laser on silicon *Optica* **5** 996–1005
[15] Kashani-Shirazi K, Vizbaras K, Bachmann A, Arafin S and Amann M-C 2009 Low-threshold strained quantum-well GaSb-based lasers emitting in the 2.5-to 2.7-μm wavelength range *IEEE Photonics Technol. Lett.* **21** 1106–8
[16] Arafin S 2012 Electrically-pumped GaSb-based vertical-cavity surface-emitting lasers *PhD Thesis* Technische Universität München Department of Electrical Engineering (available at: https://mediatum.ub.tum.de/1086591)
[17] Ansys *Lumerical* (Available at: www.lumerical.com/ansys/)
[18] Andrade N 2022 Single-mode waveguide coupling of optical antenna-LED for optical interconnects *PhD Thesis* University of California Department of Electrical Engineering and Computer Sciences (available at: https://www2.eecs.berkeley.edu/Pubs/TechRpts/2022/EECS-2022-19.html)
[19] Arafin S, Bachmann A and Amann M-C 2011 Transverse-mode characteristics of GaSb-based VCSELs with buried-tunnel junctions *EEE J. Sel. Top. Quantum Electron.* **17** 1576–83
[20] Chrostowski L and Hochberg M 2015 *Silicon Photonics Design: From Devices to Systems* (Cambridge University Press)
[21] Heidelberg Instruments *MLA150* (Available at: https://heidelberg-instruments.com/)
[22] Ulrich R 1975 Image formation by phase coincidences in optical waveguides *Opt. Commun.* **13** 259–64
[23] Singh G, Yadav R P and Janyani V 2012 Modeling of a high-performance multimode interference optical switch using reconfigurable image modulated region *Opt. Eng.* **51** 074006
[24] Okamoto K 2021 *Fundamentals of Optical Waveguides* (Academic)
[25] Min D-S, Langer D W, Pant D K and Coalson R D 1997 Wide-angle low-loss waveguide branching for integrated optics *Fiber Integr. Opt.* **16** 331–42
[26] Zhang Y, Yang S, Lim A E-J, Lo G-Q, Galland C, Baehr-Jones T and Hochberg M 2013 A compact and low loss Y-junction for submicron silicon waveguide *Opt. Express* **21** 1310–6
[27] Dwivedi S, Pinna S, Moreira R, Liu Y, Song B, Estrella S, Johansson L and Klamkin J 2018 Multicore fiber link with SiN integrated fan-out and InP photodiode array *IEEE Photonics Technol. Lett.* **30** 1921–4
[28] Nambiar S, Sethi P and Selvaraja S K 2018 Grating-assisted fiber to chip coupling for SOI photonic circuits *Appl. Sci.* **8** 1142
[29] Thorlabs *Fluoride Glass Optical Fiber* (Available at: www.thorlabs.com/newgrouppage9.cfm?objectgroup_id=7062)

Supplementary Materials for

Design of GaSb-based Monolithic Passive Photonic Devices at Wavelengths Above 2 µm

Md Saiful Islam Sumon, Shrivatch Sankar, Weicheng You, Imad I. Faruque, Sarvagya Dwivedi, and Shamsul Arafin*

*Author to whom any correspondence should be addressed.

E-mail: arafin.1@osu.edu

In this supplementary material, we provide a comprehensive overview of the optimization procedures employed for the passive photonic devices designed in our paper. We present step-by-step descriptions of the optimization processes carried out for each device. Furthermore, we highlight the key findings and insights derived from these optimization procedures, shedding light on the performance enhancement of the devices.

1. Directional coupler optimization:

The design of the directional couplers was optimized using the finite difference eigenmode (FDE) and eigenmode expansion (EME) solver of Ansys Lumerical. More simulation and analysis details can be obtained in [1]. To obtain optimized directional couplers in the monolithic GaSb-platform, the following steps were implemented:

1.1 Supermode calculation: The supermode profiles of the waveguides were calculated using the eigenmode solver by using two abruptly placed waveguides as shown in Figure S1(a). The symmetric and antisymmetric supermodes are shown in Figures S1(b) and (c), respectively. Their calculated effective refractive indices are 3.6273 and 3.624 and the index difference, $\Delta n = 0.0033$. Thus, coupling length $L'_{50\%} = \lambda/(4\Delta n) = 196$ µm at 2.56 µm, which is also confirmed by the coupling power ratio vs. coupling length curve shown in Figure S1(d).

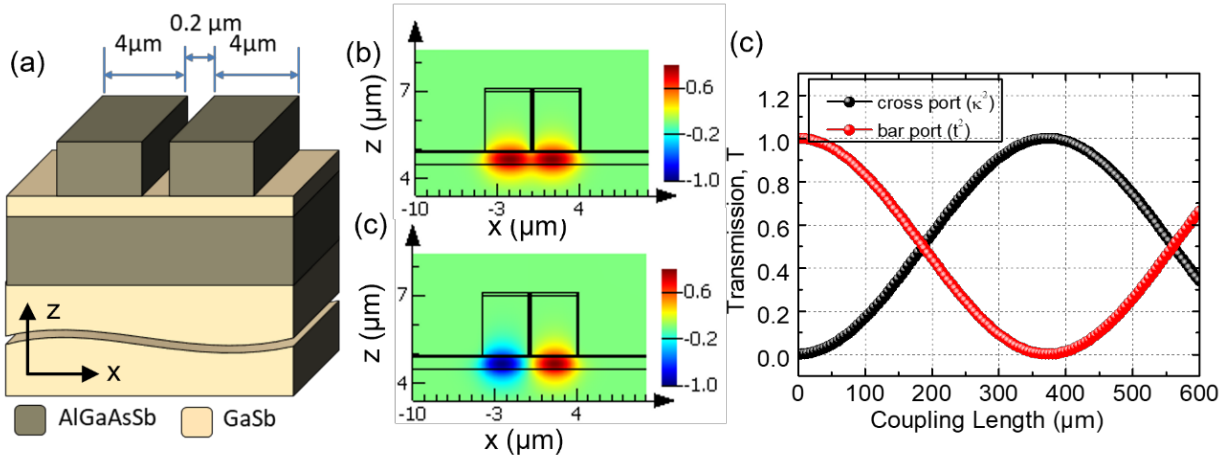

Figure S1: (a) Two waveguides placed 0.2 µm apart abruptly, (b) symmetric supermode, (c) antisymmetric supermode, (d) coupling power ratio, κ^2 as a function of coupling length.

1.2 Effective extra length calculation due to bends: For light splitting/combining, a bend is required that increases the length of a directional coupler compared to the abruptly placed ones

as shown in Figure S2(a). The EME solver was used to determine the effective extra length due to bends. We used cubic Bézier curves to define our s-shaped bends as shown in Figure S2(b), which helped optimize the S-bends only with the change of length when the S-bend width, W_s was specified. The transmission vs S-bend length L_{s_DC} is shown in Figure S2(c). It was found that a nonparallel section length of 130 µm provides almost lossless S-bends when the gap between the waveguide varies from 0.2 µm to 8 µm. For a 130 µm long non-parallel section, a length of L_p = 142 µm of the parallel section provides 50:50 coupling as suggested by T vs parallel section plot in Figure S2(d). Thus, the actual length of the DC $L_{50\%}$ coupler becomes 272 µm.

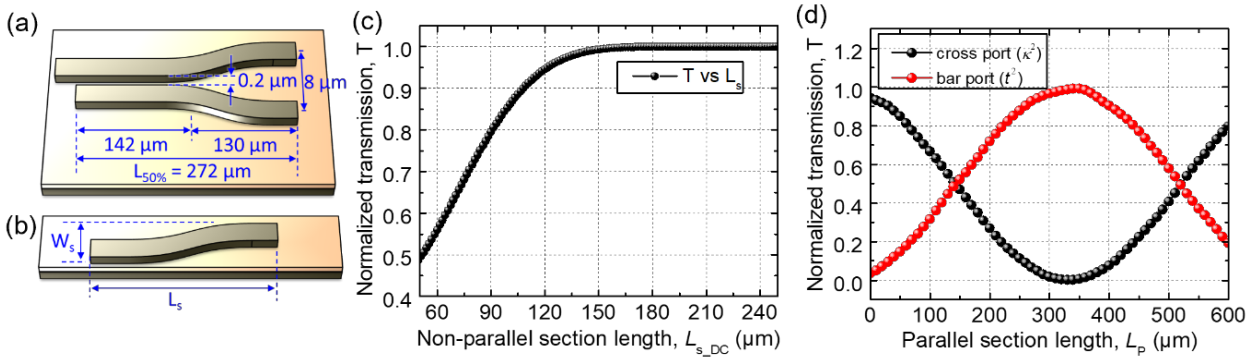

Figure S2: (a) Directional couplers with parallel waveguides and non-parallel bend sections, (b) cubic Bézier curve representing S-bends, (c) transmission vs bend section length at 2.56 µm, and (d) transmission vs DC parallel section length.

Subtracting $L'_{50\%}$ from $L_{50\%}$, we get an effective extra length due to bends, L_{bned} = 76 µm. It should be noted that the effective extra length due to bends L_{bend} is different from the S-bend length L_s.

2. Multimode interferometer coupler optimization:

The optimization process for the multi-mode interference (MMI) couplers involved several steps to achieve efficient power splitting. Further details of the steps can be obtained from [2].

2.1 Theoretical calculation of the dimension:

The initial step is to perform a numerical calculation of the effective index of the multimode section using the eigenmode solver to simplify the 3D structure to a 2D one as shown in Figure S3(a).

$$L_{MMI} = \frac{n_{\text{eff,y}} \times W_{\text{MMI}}^2}{\lambda} \qquad (S1)$$

$$L_{1\times N} = \frac{L_{\text{MMI}}}{N} + \Delta L \qquad (S2)$$

$$x_i = \left(\frac{N+1}{2} - i\right) \times \frac{W_{MMI}}{N} \;\; ; \;\; i = 1, 2 \qquad (S3)$$

$$s = \frac{W_{MMI}}{N} \qquad (S4)$$

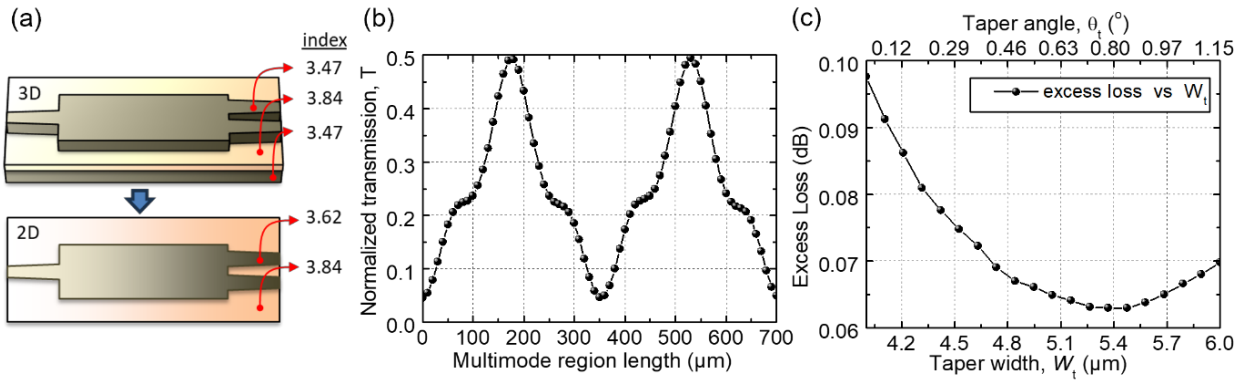

Figure S3: (a) 3D to 2D conversion of the MMI using effective index of the multimode section, (b) transmission as a function of multimode section length, (c) antisymmetric supermode, (d) coupling power ratio as a function of taper width or taper angle.

where

L_{MMI} = analytical self-imaging length;
$n_{eff,y}$ = effective index of the slab waveguide formed in the transverse direction at the core;
W_{MMI} = multimode region width;
$L_{1\times N}$ = length at which N number of images are formed;
ΔL = extra effective length to compensate the Goos- Hänchen effect;
x_i = position of the i^{th} output arms in the split section;
s = separation between the output arms;

Using Equation S2, we get L_{MMI} as 318.5 μm for W_{MMI} = 15 μm at λ = 2.56 μm. For 50:50 splitting, N = 2. Thus, L_{MMI} / 2 = 159.25 μm is the length of the multimode section that gives 50:50 splitting. This was further corrected by ΔL due to the Goos-Hänchen effect [2,3]. ΔL was obtained in the next section using Equation S2. Equation S4 gives the position of output arm x_1 and x_2 as 3.75 μm and -3.75 μm, respectively with a spacing of 7.5 μm obtained from equation S5.

2.2 Goos-Hänchen effect:

The core length of the MMI coupler was varied to investigate the Goos-Hänchen effect due to the slight penetration of mode into the cladding region using the EME solver. By analyzing normalized transmission vs. the multimode region length curve shown in Figure S3(b), the optimal core length for desired power splitting was determined to be 176 μm. Thus, using equation S2, the excess length ΔL considered to compensate the Goos-Hänchen effect was calculated to be 16.7 μm.

2.3 Input and output arm taper optimization:

The width or the angle of the tapers in the MMI coupler's input and output arms was systematically varied to optimize the coupling efficiency. By sweeping the taper width $W_{t\_MMI,}$ and analyzing the corresponding excess loss, the optimal taper width for low-loss power splitting was calculated to be 5.37 μm as shown in Figure S3(c).

3. Y-branch coupler optimization:

In order to achieve efficient power splitting with minimized loss, our design process for the Y-branch splitter involved optimizing both the taper- and S-bend sections as shown in Figure S4(a).

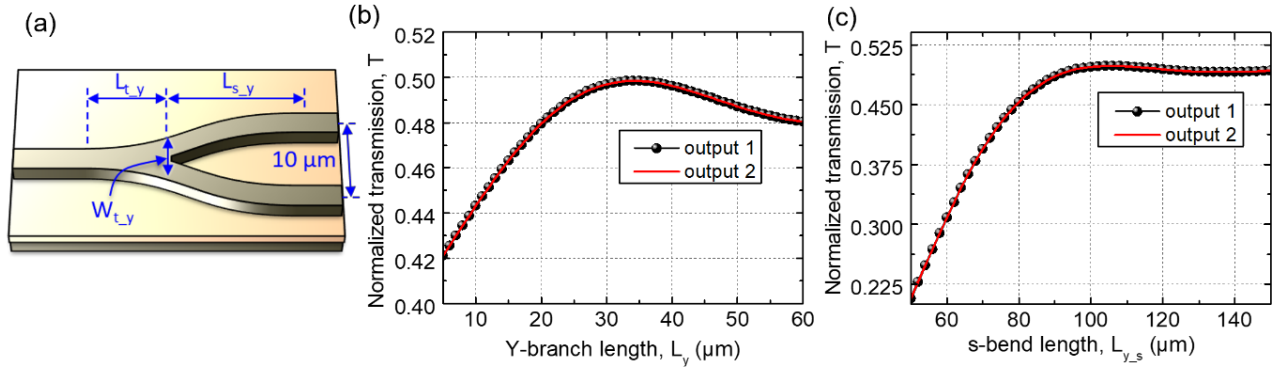

Figure S4: (a) 3D schematic of the y-branch, (b) transmission as a function of the Y-branch length, (c) transmission as a function of Bézier s-bend length or taper length.

3.1 Taper section optimization: The taper section of the Y-branch was optimized to ensure smooth and efficient power transfer between the input waveguide minimizing the back-reflection. The taper length, L_{t_y} was varied keeping the width, W_{t_y} to be 8.2 µm to achieve the desired power splitting with minimized back reflections and losses. The normalized transmission vs L_{t_y} shown in Figure S4(b) provides a maximum transmission at a taper section length of 35 µm.

3.2 Bend section optimization: The S-bend section where the waveguides curve to connect the taper section with the output waveguides was optimized to minimize mode mismatch and maintain the low loss. The curvature and length of the S-bend were adjusted to reduce bending losses and maintain the desired power distribution. Keeping L_{t_y} fixed at 35 µm, the cubic Bézier curves representing the S-bends were optimized for an output arm separation of 10 µm. The T vs L_{s_y} curve is shown in Figure S4(c). An s-bend length of 105.5 µm is found to maximize the transmission and provides 50:50 power splitting.

4. Grating coupler optimization:

The optimization process for the grating coupler involved several steps to achieve efficient coupling of light between the waveguide and the external medium and vice versa. The following steps were executed to get the optimized grating coupler in buried channel waveguides where the core is fully-etched:

4.1 Taper section optimization in EME: The taper section of the grating coupler (GC) shown in Figure S5(a) was optimized using the EME solver. We optimized the taper length for low-loss conversion of the mode size from 4 µm to 15 µm as shown in Figure S5(b) and Figure S5(c) respectively. The taper length L_{s_gc} was varied by keeping the width of the left and right arm fixed to ensure a smooth and efficient transition of light from the waveguide to the grating

structure. The transmission vs taper length curve is shown in Figure S5(d). A taper length of 120 µm provides a 96% transmission of the input light and even higher transmission can be achieved if the taper length is more than 200 µm. However, we considered 120 µm, as a lower taper length provides a lower radius of curvature of the focused grating that eventually allows for achieving a compact grating coupler.

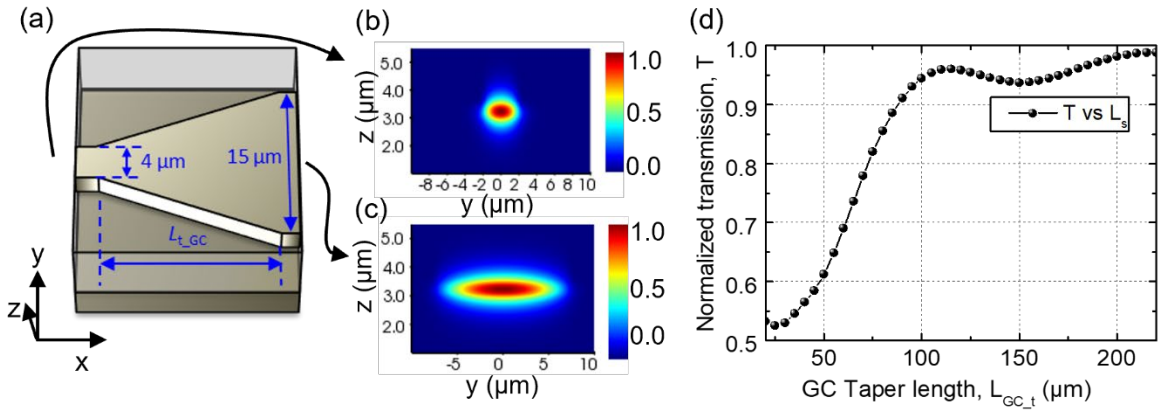

Figure S5: (a) Linear taper between the waveguide section to the grating section, (b) corresponding mode as indicated, (c) transmission vs taper length for the grating coupler.

4.2 Grating period and angle of incidence optimization using FDTD: The grating period and angle of incidence were optimized using the finite-difference time-domain, FDTD method keeping the etch depth fixed. By varying these parameters and analyzing the coupling efficiency, the optimal grating period and angle of incidence were determined. Figure S6(a) shows the coupling efficiency contour of the grating coupler with different grating periods and angles of incidence on the grating. From the contour, a grating period of 1.13 µm provides maximum coupling efficiency ~26% when light is incident on the grating region at an angle of 22°.

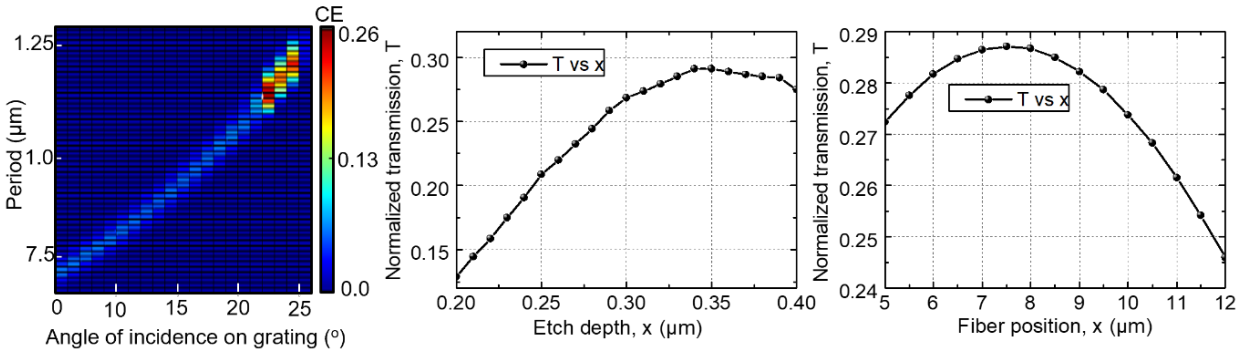

Figure S6: (a) Coupling efficiency contour for different grating periods and angle of incidence on the grating, (b) transmission vs etch depth, (c) transmission vs fiber position from the beginning of the grating and end of the taper section.

4.3 Etch depth optimization: The etch depth of the grating region was optimized to achieve strong coupling between the waveguide and the external medium. By varying the etch depth and analyzing the coupling efficiency, the optimal etch depth was determined to be 0.35 µm from Figure S6(b).

4.4 Fiber position optimization: The position of the fiber relative to the beginning of the grating region was optimized to achieve efficient light coupling. By adjusting the fiber position and analyzing the coupling efficiency, the optimal fiber position was determined to maximize the power transfer. Figure S6(c) shows that maximum coupling efficiency of 28.7% can be obtained when the fiber core center is placed 7.5 μm away from the starting of the grating region.

Reference:

[1] Chrostowski L and Hochberg M 2015 Silicon photonics design: from devices to systems: Cambridge University Press, Cambridge, UK

[2] Okamoto K 2021 Fundamentals of optical waveguides: Academic Press, Burlington, MA, USA

[3] A. W. Snyder and J. D. Love, "Goos-Hänchen shift," Applied optics, vol. 15, no. 1, pp. 236-238, 1976.